

Article

Green Anisole Solvent-Based Synthesis and Deposition of Phthalocyanine Dopant-Free Hole-Transport Materials for Perovskite Solar Cells

Suresh K. Podapangi^{1,†}, Laura Mancini^{2,†}, Jie Xu¹, Sathy Harshavardhan Reddy¹ , Aldo Di Carlo^{1,3}, Thomas M. Brown¹ and Gloria Zanotti^{2,*} 

¹ C.H.O.S.E. (Centre for Hybrid and Organic Solar Energy), Department of Electronic Engineering, University of Rome-Tor Vergata, via del Politecnico 1, 00133 Rome, Italy; suresh.podapangi@uniroma2.it (S.K.P.); xuxjie01@uniroma2.it (J.X.); sathy@ing.uniroma2.it (S.H.R.); aldo.dicarlo@ism.cnr.it (A.D.C.); thomas.brown@uniroma2.it (T.M.B.)

² Istituto di Struttura della Materia—CNR (ISM-CNR), Area della Ricerca Roma 1, Via Salaria km 29.300, 00015 Monterotondo, Italy; laura.mancini@mli.ism.cnr.it

³ Istituto di Struttura della Materia—CNR (ISM-CNR), Area della Ricerca di Roma Tor Vergata, Via del Fosso del Cavaliere 100, 00133 Rome, Italy

* Correspondence: gloria.zanotti@cnr.it; Tel.: +39-0690672318

† These authors contributed equally to this work.

Abstract: Perovskite Solar Cells (PSCs) have attracted attention due to their low cost, easy solution processability, high efficiency, and scalability. However, the benchmark expensive hole transport material (HTM) 2,2',7,7'-tetrakis[N, N-di(4-methoxyphenyl)amino]-9,9'-spirobifluorene (Spiro-MeOTAD), which is traditionally solution-processed with toxic solvents such as chlorobenzene (CB), dichlorobenzene (DCB), or toluene, is a bottleneck. To address this issue, this work investigates the implementation of Zn(II), Cu(II), or Co(II) tetra-*tert*-butylphthalocyanines (TBU4-Cu, TBU4-Zn, TBU4-Co), established macrocyclic derivatives whose synthesis and processing inside the devices have been redesigned to be more environmentally sustainable and cost-effective by substituting conventional solvents with greener alternatives such as anisole, propane-1,2-diol, and their mixture, as dopant-free HTMs in planar n-i-p PSCs. The anisole-processed HTMs provided power conversion efficiencies (PCE) up to 12.27% for TBU4-Cu and 11.73% for TBU4-Zn, with better photovoltaic parameters than the corresponding cells made with chlorobenzene for which the best results obtained were, respectively, 12.22% and 10.81%.

Keywords: hybrid perovskites; anisole; propylene glycol; green synthesis; porphyrinoids



Citation: Podapangi, S.K.; Mancini, L.; Xu, J.; Reddy, S.H.; Di Carlo, A.; Brown, T.M.; Zanotti, G. Green Anisole Solvent-Based Synthesis and Deposition of Phthalocyanine Dopant-Free Hole-Transport Materials for Perovskite Solar Cells. *Energies* **2023**, *16*, 3643. <https://doi.org/10.3390/en16093643>

Academic Editors: Luísa Andrade and Vera C.M. Duarte

Received: 16 March 2023

Revised: 15 April 2023

Accepted: 21 April 2023

Published: 24 April 2023



Copyright: © 2023 by the authors. Licensee MDPI, Basel, Switzerland. This article is an open access article distributed under the terms and conditions of the Creative Commons Attribution (CC BY) license (<https://creativecommons.org/licenses/by/4.0/>).

1. Introduction

In 2009, a new class of material called hybrid perovskites opened the doors to advanced-generation photovoltaic devices. In less than fifteen years, the power conversion efficiency (PCE) of perovskite solar cells geared up from 3.8% [1] to 25.7% [2]. Despite this impressive result, there are still important issues to be resolved to allow this technology to enter the photovoltaic market [3,4], such as improving the long-term stability of the solar cells and solving issues related to the lead (Pb) content of perovskites. Furthermore, it is necessary to find concrete alternatives to Spiro-MeOTAD, which is the benchmark hole transport material for highly performing devices but is expensive and requires chemical doping, detrimental to the stability of the perovskite layer, to be effective. In fact, doping with additives, such as cobalt complexes, Li-Bis(trifluoromethanesulfonyl)imide (Li-TFSI), or *tert*-butylpyridine (tBP), followed by atmospheric O₂ exposure [5–8], is required to increase the optoelectrical properties of such HTMs. These dopants are hydrophilic and, given the perovskite active layer degradation in the presence of moisture, the resulting solar cell stability is hindered [9]. To avoid degradation and improve the stability of the

devices, the development of dopant-free hole transport materials (HTMs) is desirable. Phthalocyanines are a well-known class of aromatic, macrocyclic, compounds that have been of interest to the scientific community for several decades. Their central cavity can host a wide variety of metal ions, while the macrocycle periphery can be functionalized to finely tune their optoelectrochemical properties and make phthalocyanines particularly attractive in solar cell applications. In 2015, V. Kumar et al. first introduced phthalocyanine as a hole transport material in perovskite solar cells with a PCE of 5% [10]. Since that first paper, many others followed, reporting PCEs >20% in both mesoscopic and planar n-i-p devices [11–16]. Given their widespread technological importance, the need to develop environmentally sustainable synthetic protocols for their preparation is increasingly urgent. To date, their synthesis in solution commonly requires a reaction media such as alkyl alcohols (pentanol, hexanol), dimethylaminoethanol (DMAE), chlorobenzene, quinoline, and α -chloronaphthalene, most of which are toxic and non-environmentally friendly. Some green synthetic approaches based on the solvothermal methods [17,18], mechanochemistry [19], or alternative sources of energy such as microwaves [20–25] and ultraviolet radiation [26,27], have been developed, while the choice of a more sustainable reaction medium has so far relied mostly on ionic liquids [28,29] and deep-eutectic solvents [30], and has moved towards greener conventional protocols only in the last few years [31,32]. In this work, we study the replacement of Spiro-MeOTAD with solution-processable, dopant-free, copper, zinc, and cobalt tetra-*tert*-butylphthalocyanines (TBU4-Cu, TBU4-Zn, TBU4-Co) of which we have developed an inexpensive synthetic protocol exploiting the green, non-toxic, non-volatile solvents propane-1,2-diol and anisole. Our choice fell on these solvents for several reasons: Anisole is a high-boiling point and biodegradable aromatic compound obtained from renewable sources, such as lignin and guaiacol [33–35], and ranks well in the solvent selection guides [36]. Propane-1,2-diol, commonly known as propylene glycol, is widely used as a food and cosmetic additive and represents a safer alternative to conventional ethylene glycol-based, anti-freezing, liquids. Furthermore, it can be produced through the chemical modification of glycerol [37,38] and its microbial synthesis [39] is currently a relevant object of study. The synthetic work on these molecules is the continuation of a first green approach to the synthesis of unsubstituted and alkyl-substituted phthalocyanines that we recently published [31], in which we were, however, unable to identify suitable reaction conditions for obtaining them with satisfactory yields. Our synthetic protocol applied to a lab-scale synthesis afforded the zinc and copper derivatives with comparable yields to the standard procedure and at a lower price than not only Spiro-MeOTAD but also their commercially available counterparts. To further mitigate the environmental impact of solvents in the development of perovskite solar cells, which conventionally rely on the harmful chlorobenzene to process charge-transport materials in the final devices, anisole was also chosen as the deposition solvent of our HTMs. While the scientific literature accounts for some studies on its use in the antisolvent step [40–43], to the best of our knowledge, only one paper reports on its use as an HTM solvent in conventional Spiro-MeOTAD-based devices [41]. Replacing chlorobenzene with anisole improved the photovoltaic parameters of all our cells, with the best results obtained with the copper derivative that scored efficiencies up to 12.27% and showed a significant reduction in the hysteresis of the related J-V curves.

2. Materials and Methods

2.1. Materials for Synthesis and Characterizations

All reagents and solvents for the chemical synthesis were purchased from Merck Life Science, TCI Chemicals, and Carlo Erba Reagents and used without further purification. Reactions were purged and refilled three times with argon, performed under an inert atmosphere, and monitored by thin-layer chromatography (TLC) employing a polyester layer coated with 250 mm F254 silica gel. Chromatographic purifications, when needed, were performed using silica gel 60A 35–70. ^1H NMR spectra were recorded on a Bruker AVANCE 600 NMR spectrometer operating at a proton frequency of 600.13 MHz

in DMSO- d_6 ; chemical shifts (δ) are given in ppm relative to TMS. Infrared spectra were recorded on a Shimadzu FT-IR prestige-21 spectrometer (Kyoto, Japan) using an attenuated total reflectance (ATR) unit. UV-Vis spectra were recorded on a Perkin-Elmer Lambda 950 UV-vis/NIR spectrophotometer using THF as a solvent. ESI-MS spectra were recorded at the Toscana Life Science facility with a Thermo Fisher Scientific Q-Exactive Plus (Geel, Belgium). The samples have been analyzed by direct infusion in a positive mode with a spray voltage of 3.5 kV, sheat gas 10 a.u., and a flow rate of 5 μ L/min. Melting points were determined using a Büchi 535 apparatus. Cyclic voltammetry (CV) measurements were carried out at 25 °C with a potentiostat-galvanostat Metrohm PGStat204 in a conventional three electrodes cell. A platinum disk (~1 mm) was used as a working electrode together with a platinum wire as an auxiliary electrode. The reference electrode was Ag/AgCl and the Fc⁺/Fc (ferrocenium/ferrocene) couple was used as an external standard. The sample solutions were $\sim 10^{-3}$ M in freshly distilled dichloromethane, and dry tetrabutylammonium hexafluorophosphate (TBAPF₆) was used as the supporting electrolyte at 0.1 M concentration. The solutions were previously purged for 10 min with nitrogen, and all measurements were performed under an inert atmosphere. The voltammograms were recorded at scan rates ranging from 0.05 to 0.1 Vs⁻¹.

2.2. Synthesis of 2,9(10),16(17),23(24)-Tetra-Tert-Butylphthalocyanines

All the reactions were performed in a two-necked 25 mL round bottom flask equipped with a reflux condenser and a magnetic stirrer.

Synthesis of TBU4-Co. 203 mg (1.10 mmol) of 4-*tert*-butylphthalonitrile, 82.9 mg (0.33 mmol) of Co(OAc)₂·4H₂O, and one Pasteur-drop (approx. 16 mg, 0.106 mmol) of DBU were stirred in 2.08 g of a solvent mixture (1.85 g propane-1,2-diol + 0.23 g anisole) under reflux overnight. The mixture was then cooled, concentrated under reduced pressure, treated with 10 mL of HCl 1N, filtered, and washed with water (8 mL) and methanol (10 mL). The resulting crude was then purified by filtration on a silica pad (10 g) with 50 mL (35.4 g) of a petroleum ether 40–70°:THF mixture. Finally, the cobalt phthalocyanine was further washed with 5 mL of methanol. The results were 69 mg (33% yield); UV/Vis (THF): λ_{\max} 324, 656 nm; IR: 2953, 2899, 2864, 1614, 1090, 826, 750; ESI *m/z* 795.84 [M]⁺; Melting point >250 °C; elemental analysis calcd (%) for C₄₈H₄₈CoN₈: C 72.44, H 6.08, N 14.08; found: C 71.73, H 5.82, N 13.62.

Synthesis of TBU4-Cu. 200 mg (1.08 mmol) of 4-*tert*-butylphthalonitrile, 60 mg (0.30 mmol) of Cu(OAc)₂·H₂O, and one Pasteur-drop (approx. 16 mg, 0.106 mmol) of DBU were stirred in 2 g of a solvent mixture (1.85 g propane-1,2-diol + 0.15 g anisole) under reflux for 6 h. The mixture was then cooled, concentrated under reduced pressure, treated with 10 mL of HCl 1N, filtered, and washed with water (10 mL) and hot methanol (2 × 10 mL). The results were 120 mg (55% yield); UV/Vis (THF): λ_{\max} 344, 671 nm; IR: 2953, 2897, 2862, 1614, 1087, 826, 746; ESI *m/z* 800.33 [M]⁺; Melting point > 250 °C; elemental analysis calcd (%) for C₄₈H₄₈CuN₈: C 72.02, H 6.04, N 14.00; found: C 71.64, H 5.80, N 13.28.

Synthesis of TBU4-Zn. 200 mg (1.08 mmol) of 4-*tert*-butylphthalonitrile, 60 mg (0.27 mmol) of Zn(OAc)₂·2H₂O, and one Pasteur-drop (approx. 16 mg, 0.106 mmol) of DBU were stirred in 2 g of a solvent mixture (1.85 g propane-1,2-diol + 0.15 g anisole) under reflux for 3 h. The mixture was then cooled, concentrated under reduced pressure, treated with 10 mL of HCl 1N, filtered, and washed with water (8 mL) and methanol (10 mL). The resulting crude was then purified by filtration on a silica pad (10 g) with 50 mL (35.4 g) of a petroleum ether 40–70°:THF mixture. Finally, the zinc phthalocyanine was further washed with 5 mL of methanol. The results were 111 mg (51% yield); ¹H NMR (600 MHz, [D₆]DMSO): δ = 9.45–9.28, (m, 8H), 8.34 (m, 4H), 1.78 (m, 36H, C-(CH₃)₃); UV/Vis (THF): λ_{\max} 348, 672 nm; IR: 2953, 2901, 2864, 1612, 1086, 827, 745; ESI *m/z* 802.83 [M]⁺; Melting point >250 °C; elemental analysis calcd (%) for C₄₈H₄₈ZnN₈: C 71.86, H 6.03, N 13.97; found: C 71.93, H 5.91, N 13.35.

2.3. Materials for Device Preparation

Tin oxide (SnO_2), 15% in H_2O colloidal dispersion, was purchased from Alfa Aesar. PbI_2 and PbBr_2 were purchased from the TCI company. FAI, MABr, CsI, dimethylformamide (DMF) (99.8%), dimethyl sulfoxide (DMSO) (99.5%), and chlorobenzene (99.8%) were purchased from Sigma Aldrich. The anisole (99.0%) was purchased from Acros. The Spiro-MeOTAD ($\geq 99.8\%$) was purchased from Borun NewMaterial Technology Ltd. (Ningbo, China). The 4-*tert*-butylpyridine (tBP) and bis(trifluoromethylsulfonyl)amine lithium salt (LiTFSI) were purchased from Sigma Aldrich and the cobalt (III) (FK209) from Lumtec.

2.4. Device Fabrication

At first, the glass/indium tin oxide (ITO) substrates (Kintec $-8 \Omega/\text{square}$, $25 \times 25 \text{ mm}$) were patterned using a raster scanning laser (Nd: YVO_4 , $\lambda = 1064 \text{ nm}$, 8 ns, pulsed at 10 kHz with a fluence of $260 \text{ mJ}/\text{cm}^2$). Then, the patterned glass/ITO substrates were stepwise cleaned in an ultrasonic bath using de-ionized water, acetone, isopropanol, and de-ionized water for 15 min each, followed by drying with an airflow. Then, cleaned substrates were transferred under UV-Ozone and treated for 15 min to enhance the wettability and remove the organic residues of the ITO surface. For the fabrication of the ITO/ $\text{SnO}_2/\text{Cs}_{0.05}(\text{MA}_{0.17}\text{FA}_{0.83})_{0.95}\text{Pb}(\text{I}_{1-x}\text{Br}_x)_3/\text{Spiro-MeOTAD}/\text{Au}$ devices, the SnO_2 precursor solution was prepared by mixing the tin oxide (SnO_2) (15% in H_2O colloidal dispersion). The SnO_2 precursor solution was spin-coated on glass/ITO substrate in ambient air at 6000 rpm for 30 s and annealed at 100°C in ambient air for 1 h. The triple cation precursor solution containing FAI (1 M), PbI_2 (1.2 M), MABr (0.2 M), PbBr_2 (0.2 M), and CsI (0.08 M) was prepared in anhydrous DMF: DMSO 3.2:1 (*v:v*). The deposition was carried out in a nitrogen-filled glovebox by spin-coating the precursor solution at 4000 rpm for 20 s; 150 mL of chlorobenzene was dropped on the substrate 15 s before the end of the spin-coating process. The Spiro-type HTM solutions were prepared by dissolving the compounds at a 73.42 mg/mL concentration in CB and stirred overnight at room temperature; 2 h prior to deposition, the HTM solutions were doped with 16.6 $\mu\text{L}/\text{mL}$ LiTFSI stock solution (530 mg/mL in acetonitrile), 26.77 $\mu\text{L}/\text{mL}$ TBP and 7.2 $\mu\text{L}/\text{mL}$ cobalt (III) complex solution (FK209 from Lumtec). The Spiro HTMs were spin-coated at 2000 rpm for 20 s, whereas the phthalocyanines (TBU4-Co, Cu, and Zn) based HTMs were prepared by dissolving them in Anisole or CB at a concentration of 10 mg/mL and spin-coated at 3000 rpm for 30 s. Finally, a 100 nm thick Au electrode was deposited by thermal evaporation.

2.5. Device Characterization

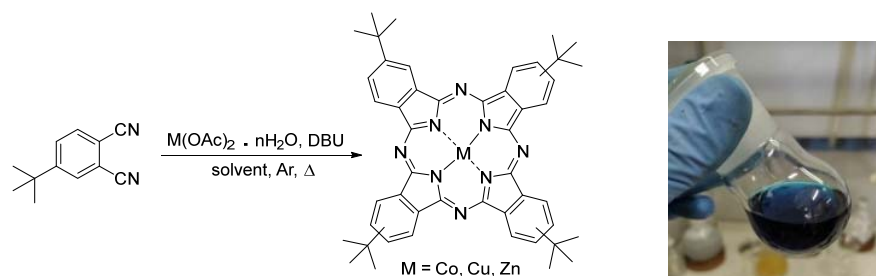
The ultraviolet-visible (UV-Vis) absorption spectra were measured using a UV-vis 2550 Spectrophotometer from Shimadzu. The images of the surface morphology of the perovskite layer were captured by the Hitachi SU8000 scanning electron microscope (SEM). The current density-voltage (J-V) of the solar cells were measured using a source meter (Keithley 2400), equipped with a calibrated solar simulator (ABET Sun 2000, class A) at AM1.5G and $100 \text{ mW}\cdot\text{m}^{-2}$ illumination at room temperature. EQE, Dark JV spectra, transient photovoltage (TPV) decay, SCLC, and PL were measured using a modular testing platform (Arkeo-Cicci Research s.r.l., Grosseto, Italy), the details can be found in a previously published paper [44]. For all the J-V characterizations, a black tape mask was employed to define an active area (0.09 cm^2) of cells.

3. Results

3.1. Synthesis of Tetra-Tert-Butylphthalocyanines

Briefly, the phthalocyanine ring is formed via the metal-templated tetramerization of a properly functionalized phthalonitrile in a reaction medium under an inert atmosphere. The synthesis of tetra-*tert*-butylmetalophthalocyanines, sketched in Scheme 1, is usually performed on 4-*tert*-butylphthalonitrile and a metal salt in refluxing DMAE. An organic

base, such as 1,8-diazabicyclo(5.4.0)undec-7-ene (DBU), is frequently used to catalyze the reaction.



Scheme 1. Synthesis of tetra-*tert*-butylphthalocyanines.

Solvents, being used in large excess with respect to the reactants, may have a great environmental impact on a synthesis. Therefore, if a solvent is flammable, irritating, toxic, or harmful, it is worth finding alternatives that are more sustainable and safer, and, at the same time, preserve the yields of the target reaction. Aiming at expanding the screening on the green solvents for the synthesis of tetra-alkyl-substituted phthalocyanines [31], we replaced DMAE with propane-1,2-diol, a green solvent with suitable physical and chemical properties. Its chemical structure is characterized by two hydroxy groups, potentially capable of assisting the tetramerization process via the coordination of the cyano groups of the phthalonitriles and the metal ion. Furthermore, its miscibility with water would have allowed its straightforward removal along with the water-soluble impurities, simplifying the purification of target phthalocyanines. Unfortunately, when dissolved in propane-1,2-diol and heated at the reaction temperature, 4-*tert*-butylphthalonitrile crystallized copiously on the walls of the flask, effectively decreasing the quantity of material available to form the expected products. Employing anisole as a co-solvent has disadvantaged this collateral process by increasing the solubility of the organic reactant, improving the overall outcome of the reaction in all cases. These modified reaction conditions successfully provided all the target molecules, which were easily purified via filtrations on short silica pads or washings with water and methanol, as detailed in the experimental section. The zinc and copper derivatives were obtained with yields comparable to the standard procedure [31], 51% and 55%, respectively, while the result for the cobalt phthalocyanine is lower. The structure of the phthalocyanines was confirmed by means of standard characterizations, such as ^1H NMR for the diamagnetic TBU4-Zn, ultraviolet-visible (UV-Vis) absorption spectra, and elemental analyses. In the proton spectrum, Figure S1 in the Supplementary Materials, the multiplicity of the $-\text{CH}_3$ signal, centered at 1.78 ppm, indicates that the zinc derivative is synthesized as a mixture of regioisomers, a common feature for tetra-substituted phthalocyanines. By extension, TBU4-Co and TBU4-Cu are most likely obtained as regioisomeric mixtures. The UV-Vis spectra of the three derivatives in tetrahydrofuran (THF), shown in Figure 1a, show the expected Q- and Soret bands in the 650–670 and 320–350 spectral regions, respectively. The absence of peaks at around 700 nm, assignable to the Q-Band of metal-free derivatives, suggests that the templating effect of the metal ions is effective in the chosen solvent mixture. The sharpness of the main absorption bands indicates the absence of aggregation phenomena, in agreement with the coordinating nature of THF. Determining the oxidation potential of the HTMs is of relevant importance to establish their compatibility with the chosen perovskite material. The cyclic voltammetric measurements performed on TBU4-Zn, TBU4-Co, and TBU4-Cu revealed values of -5.13 eV, -4.93 eV, and -5.10 eV, respectively (Supplementary Materials Figure S4a–c). Such values theoretically allow the implementation of these phthalocyanines with several perovskite compositions, as the graphical representation of the energy level arrangement for TBU4-Co, TBU4-Cu, and TBU4-Zn in the n-i-p architecture shown in Figure 1b suggests.

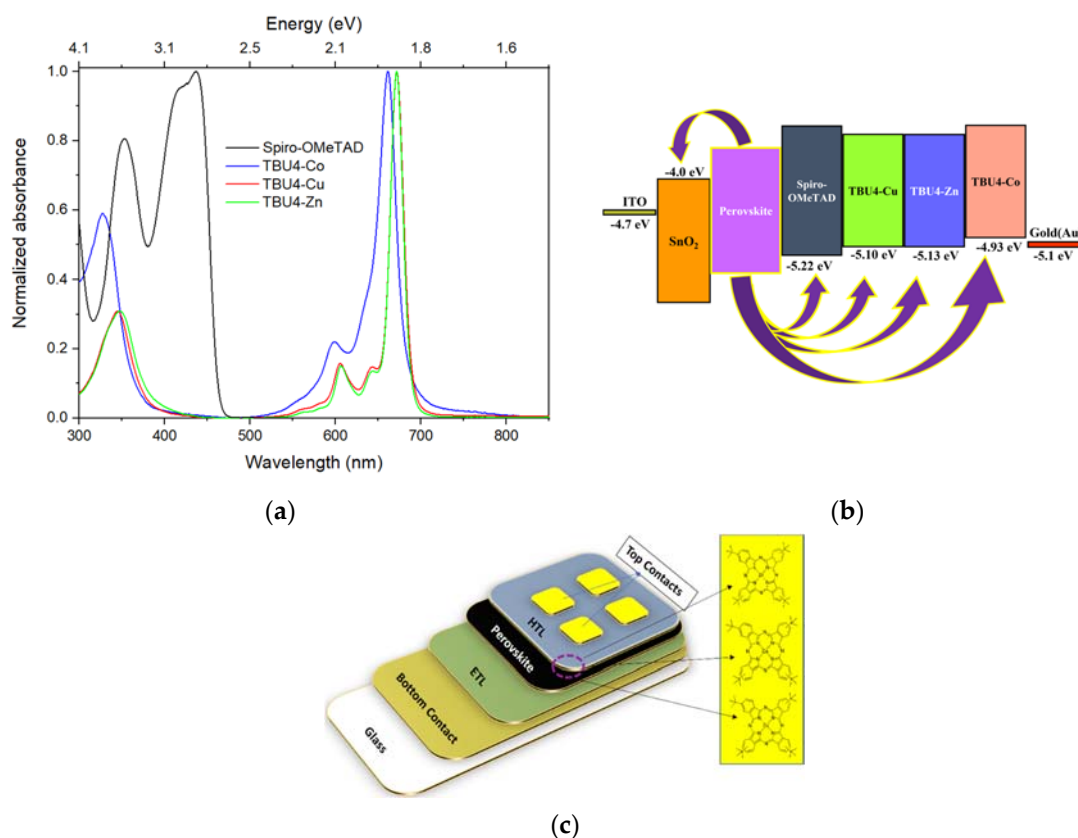


Figure 1. (a) UV-Vis spectra of Spiro (black curve) TBU4-Co (blue curve), TBU4-Cu (red curve), and TBU4-Zn (green curve) in THF; (b) Schematic of the energy level arrangement for doped Spiro-MeOTAD, TBU4-Co, TBU4-Cu, and TBU4-Zn in n-i-p architecture; (c) Schematic diagram of device stack and phthalocyanines molecule.

The environmental sustainability of a chemical synthesis can be assessed using the E-factor, which is the ratio of the mass of waste per mass of product. While there are some examples in porphyrin chemistry [45–47], a first step in the evaluation of some synthetic approaches to phthalocyanine derivatives has been performed only very recently [48]. The E-factors of our syntheses are reported in Table 1.

Table 1. Yields and E-factors for the synthesis of TBU4-Co, TBU4-Cu, and TBU4-Zn.

HTM	Yield (%)	E-Factor
TBU4-Co	33	1125
TBU4-Cu	55	317
TBU4-Zn	51	698

From the comparison with the syntheses reported in [48], for which in some cases the E-factor is <100, the calculated values for our derivatives are quite high given the one-step nature of the synthesis-related processes, but it is worth pointing out that any substance, including water and low-hazardous chemicals that make up most of our waste, is considered in the calculation. Furthermore, the synthesis of the phthalocyanines in solution often requires careful and time-consuming purification, even managing to avoid chromatography, as in the case of TBU4-Cu. Lastly, we did not adopt any strategy of solvent recovery which may have mitigated the impact of separating the target products from the impurities on the final values. As a general remark, most wastes are clearly due to workups and purifications, suggesting the need to work on their optimization as much as on the syntheses to further increase the environmental sustainability of the entire process.

Consistently with this observation, the copper derivative has the lowest E-factor, given its straightforward purification step.

3.2. J-V Characterization, IPCE, and Statistical Evaluation

The three HTMs were tested in a planar perovskite solar cell (n-i-p) with the glass/ITO/SnO₂/FAMACs/HTM/Au architecture shown in Figure 1c, without any dopants. To the best of our knowledge, even though the *tert*-butylphthalocyanines have been employed as p-type materials in mesoscopic perovskite solar cells, they have never been reported in such planar structures.

A batch of doped Spiro-MeOTAD-based cells (reference Spiro), has been prepared and measured for comparison. The main photovoltaic parameters of the tested devices are reported in Table 2.

Table 2. Photovoltaic parameters of perovskite solar cells with CB- and anisole-processed HTMs, measured under standard test conditions (AM1.5G, 1000 W/m²). Values for the best devices are reported in round brackets.

Device Name	V _{oc} [V]	J _{sc} [mAcm ⁻²]	FF [%]	PCE [%]
Spiro-MeOTAD in anisole	0.96 ± 0.01 (0.97)	20.48 ± 0.36 (20.56)	64.87 ± 4.95 (71.46)	12.68 ± 0.97 (14.23)
Spiro-MeOTAD in CB	1.000 ± 0.01 (1.011)	21.09 ± 0.15 (21.25)	71.55 ± 0.88 (72.29)	15.11 ± 0.18 (15.30)
TBU4-Cu in Anisole	0.90 ± 0.014 (0.92)	19.38 ± 0.41 (19.98)	67.46 ± 2.07 (69.77)	11.76 ± 0.32 (12.27)
TBU4-Cu in CB	0.90 ± 0.01 (0.91)	19.27 ± 0.26 (19.67)	66.38 ± 1.99 (68.24)	11.53 ± 0.37 (12.22)
TBU4-Zn in Anisole	0.917 ± 0.022 (0.95)	19.101 ± 0.426 (19.56)	64.516 ± 1.379 (66.14)	11.296 ± 0.334 (11.73)
TBU4-Zn in CB	0.906 ± 0.021 (0.93)	18.804 ± 0.487 (19.38)	61.44 ± 2.328 (63.54)	10.46 ± 0.201 (10.81)
TBU4-Co in Anisole	0.876 ± 0.013 (0.88)	15.626 ± 0.531 (16.26)	58.82 ± 1.730 (61.13)	8.06 ± 0.432 (8.83)
TBU4-Co in CB	0.865 ± 0.012 (0.87)	15.766 ± 0.532 (16.31)	59.238 ± 1.455 (61.09)	8.091 ± 0.480 (8.62)

Reference Spiro cells delivered an average PCE of 15.11% (PCE_{MAX} = 15.30%) with CB as a solvent, which dropped to 12.68% (PCE_{MAX} = 14.23%) when using anisole. TBU4-Cu processed with CB yielded an average PCE of 11.53% (PCE_{MAX} = 12.22%) and comparable results were obtained with anisole, with an average PCE of 11.76% (PCE_{MAX} = 12.27%). The CB-processed TBU4-Zn cells showed slightly lower values than the copper derivative, with an average PCE of 10.46% (PCE_{max} = 10.81%), while the use of anisole raised the average PCE to 11.29% (PCE_{max} = 11.73%). The TBU4-Co-based devices performed poorly in both solvents, with an average PCE of 8.06% (PCE_{MAX} = 8.83%) in anisole. There are two main reasons for this evidence: The misalignment between the oxidation potential of TBU4-Co (−5.04 eV) and the gold counter electrode (−5.1 eV), shown in Figure 1b, prevents an efficient collection of charge carriers [49], resulting in a decrease in the cell parameters. Conversely, a favorable alignment of Cu-TBU4 and Zn-TBU4 accounts for their better performances. Furthermore, the insufficient performances of TBU4-Co could depend on the poor uniformity of the hole transport layer, as suggested by the SEM images that will be discussed later. As a general remark, the phthalocyanine-based HTMs gave lower efficiencies when compared to the Spiro-MeOTAD, but it is worth pointing out that chemical doping might have a relevant impact on this discrepancy. Nevertheless, TBU4-Cu and TBU4-Zn are promising alternative HTMs in planar dopant-free devices, in fact, the values obtained for the best cells are in line with a recent literature survey [50] according to which photovoltaic devices based on the very same perovskite phase can give PCEs in the 12–20% range. Furthermore, their efficiency values do not alter much by changing

the solvent, contrary to what happens to the reference Spiro cells for which, moreover, the use of additives is essential to obtain good performances. Additionally, anisole-processed TBU4-Cu gives a nice hysteresis-free J-V curve, as shown in Figure S7b in the Supporting Information, likely due to the formation of a favorable energy level alignment at the perovskite/HTM interface. To account for the generally better results obtained in anisole, we suggest that, in line with the previous studies on the deposition of phthalocyanine HTMs with aromatic solvents [51], the boiling point of anisole promotes a better quality of the resulting films. Compared to chlorobenzene, whose bp is 131–132 °C, anisole boils at a higher temperature, 154–155 °C precisely. This results in slower solvent evaporation during the spin-coating process, which allows the phthalocyanine molecules to form a more homogeneous film on the perovskite surface. Because of this, an improvement in the fill factor is expected, which, in fact, is found both in the copper and the zinc derivative.

The results of the devices J-V characterization at STC (AM1.5G, 100 mW/cm², 25 °C) are shown in Figure 2a, the statistical evaluation graph of the anisole-based devices is shown in Figure 2c, while Figure 2d shows the ratio of the average PCE of anisole and chlorobenzene-based devices. The values > 1 obtained by TBU4-Cu and TBU4-Zn suggest that these HTMs worked even better in anisole solutions. The external quantum efficiency (EQE) was evaluated to analyze the different spectral conversion efficiency for the three different HTMs. As shown in Figure 2b, the EQE spectra have a similar shape for the three materials. An EQEs above 80% were observed for the reference Spiro cells and TBU4-Cu-based cells, while the TBU4-Zn and TBU4-Co HTM delivered a lower EQE. The integrated J_{SC} determined from the EQE spectrum was within the experimental error (5% discrepancy) for the reference Spiro cells (integrated J_{SC} = 21.09 mW/cm², J_{SC} = 20.56 mW/cm² under the sun simulator) and TBU4-Cu cells (19.27 mW/cm² vs. 19.98 mW/cm²).

The reliability of these HTMs was further tested by measuring the stabilized photocurrents near the maximum power point of the corresponding devices shown in Figure 3a,b. The stabilized power outputs were calculated by multiplying the photocurrent and photovoltage, yielding a steady-state PCE of 14.2% for Spiro and 12.2% for TBU4-Cu, very close to the measured PCE, thus, indicating the high reliability of the chosen materials.

Dark current-voltage (J-V), or reverse bias J-V, is a phenomenon where the J-V curve is measured in reverse bias. When the electric field is reversed, it measures the cell's capacity to transport charge. It is often used to measure the quality and stability of the perovskite solar cells, as it measures how efficiently the cell can transport charge.

Dark J-V can be used to study the kinetics of charge transport and recombination in the cell, as well as the quality of the interfaces between the perovskite layer and other layers in the cell. Figure 4a compares the dark current-voltage characteristics of the devices with different HTMs. The reference Spiro exhibits the smallest leakage current density in the reverse bias region, followed by the TBU4-Cu- and TBU4-Zn-based devices.

The TBU4-Co-based device exhibits more leakage current compared with the other phthalocyanines, which suggests an increased charge carrier recombination by high series resistance [52,53]. The peak voltage of the perovskite solar cells, with different HTMs, can be different due to the difference in their energy levels. The difference in the position of the smallest leakage current density, depending on the HTM, can be attributed to the difference in energy level alignment between the latter and the perovskite [54]. The graph shows the dark J-V curves of the solar cells with the HTMs to probe the current flow ability. The graph is divided into four regions, I, II, III, and IV, which correspond to the shunt current region, recombination current in a diode space-charge region, diffusion current, and diffusion current limited by series resistance, respectively. The inflection point at 0.7 V is due to the recombination current in a diode space-charge region. The space-charge recombination is due to the potential differences in the various HTMs and metal contact. This effect is more pronounced in TBU4-Co due to more recombination currents and less pronounced in the other HTMs.

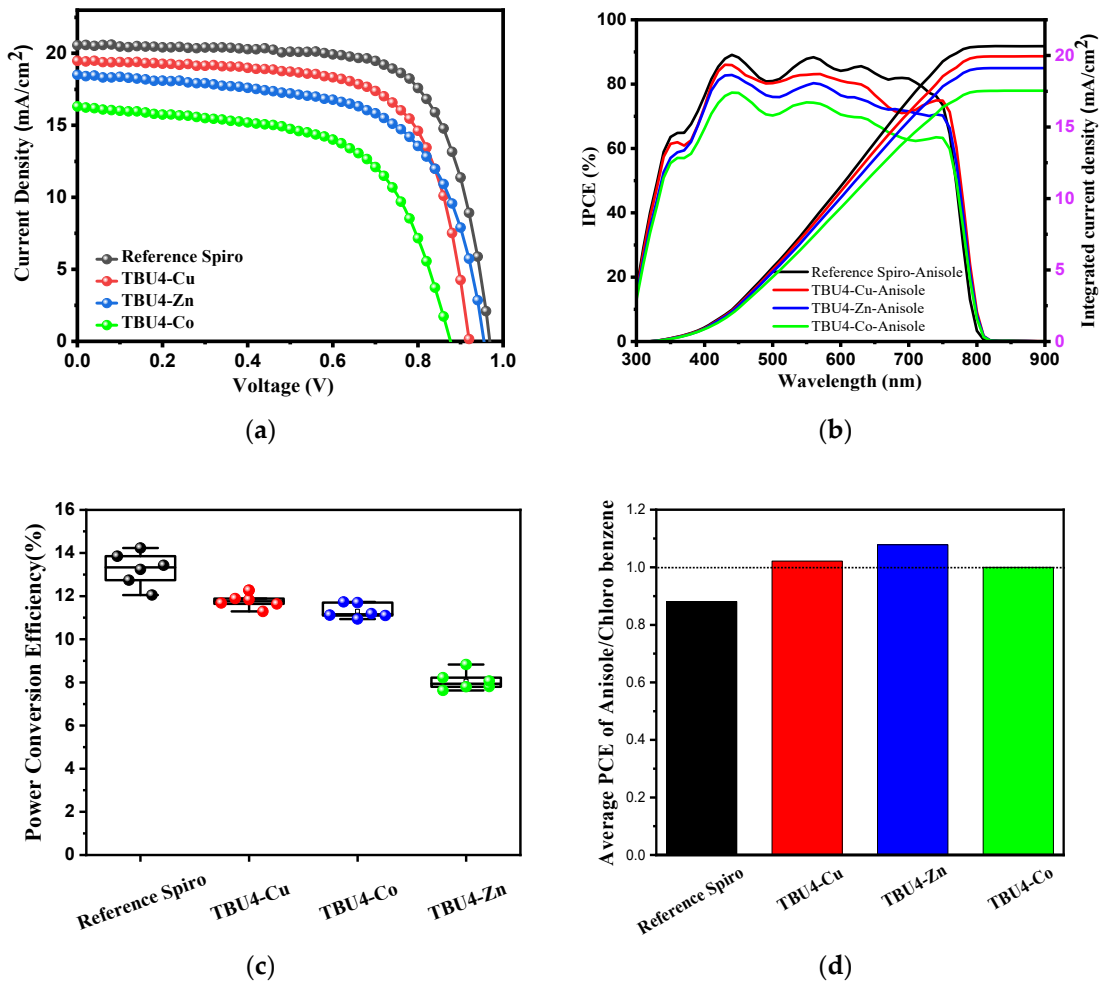


Figure 2. (a) Current density vs. voltage curves of the best anisole-based glass/ITO/SnO₂/FAMACs/HTM/Au cells with reference spiro-MeOTAD (black curve), TBU4-Cu (red curve), TBU4-Zn (blue curve) and TBU4-Co (green curve); (b) IPCE spectra of the perovskite solar cells based on various anisole-processed HTMs; (c) Anisole-based devices statistical evaluation box charts (6 samples for each); (d) Ratio of Average PCEs of anisole- and chlorobenzene-based devices.

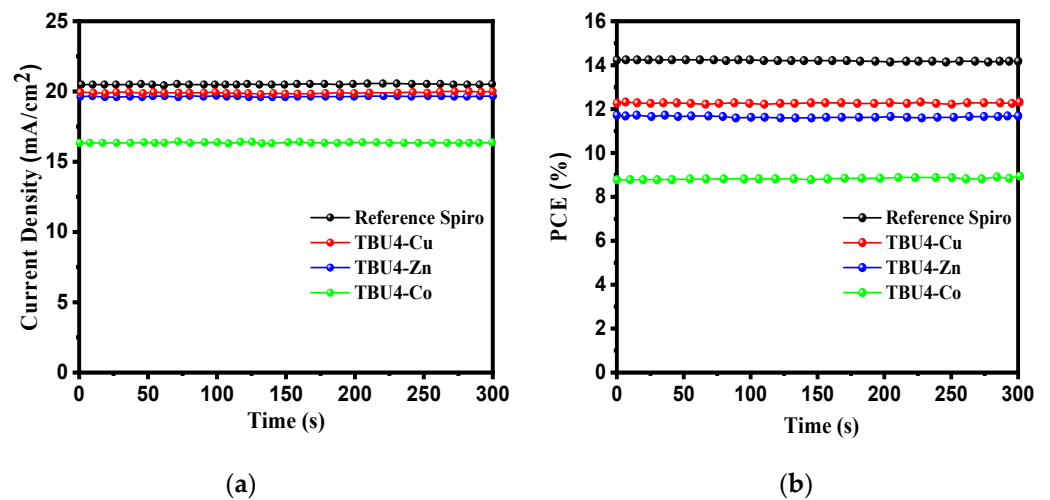


Figure 3. Stabilized (a) photocurrent density and (b) PCE measured under a bias near the maximum power point.

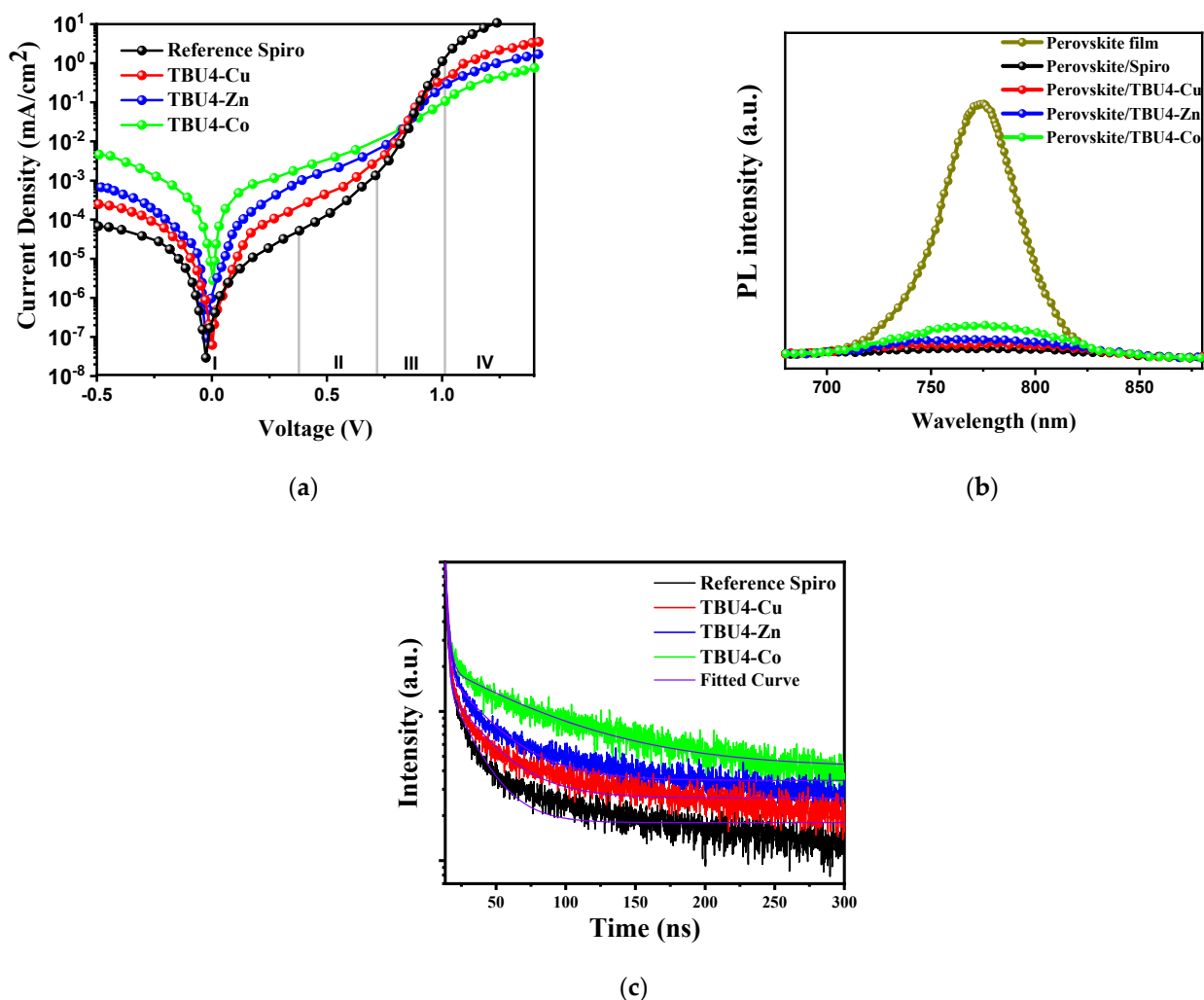


Figure 4. (a) Dark current-voltage characteristics of Spiro-MeOTAD (black curve), TBU4-Cu (red curve), TBU4-Zn (blue curve), and TBU4-Co (green curve) plotted on a semi-logarithmic scale; (b) Steady-state PL spectra of perovskite (brown curve), perovskite/Spiro-MeOTAD (black curve), perovskite/TBU4-Co (green curve), perovskite/TBU4-Zn (blue curve), and perovskite/TBU4-Cu (red curve). (c) TRPL spectra of samples with a structure of glass/perovskite/HTMs (Spiro, TBU4-Cu, TBU4-Zn, TBU4-Co).

Photoluminescence (PL) quenching at the perovskite/HTM interface was investigated to examine the hole-accepting capabilities of the HTMs. An efficient quenching of the steady-state PL and a reduction of the PL lifetime indicate an efficient charge extraction at the perovskite/HTM interface. The PL spectra reported in Figure 4c demonstrate that both TBU4-Cu and TBU4-Zn effectively quench the perovskite emission signal, the former having a slightly higher quenching efficiency than the latter. On the contrary, TBU4-Co showed poorer quenching, consistent with its lower photovoltaic performances in the device.

To further investigate the impact of our HTMs on charge transport properties in perovskite films, time-resolved photoluminescence (TRPL) measurements were conducted, as depicted in Figure 4c.

The TRPL samples were prepared on glass substrates with the structure of the glass/perovskite/HTMs. We fitted the PL decay curves by using a bi-exponential decay function as shown below [55]:

$$I(t) = A_1 \exp\left(-\frac{t}{\tau_1}\right) + A_2 \exp\left(-\frac{t}{\tau_2}\right)$$

The smaller time constant, τ_1 , represents bimolecular recombination, while the larger time constant, τ_2 , represents the lifetime of charge carriers in the perovskite film. The PL decay amplitudes, A_1 and A_2 , are also associated with these time constants. Table 3 displays the PL decay times and amplitudes obtained from fitting the PL decay curves.

Table 3. Summary of the parameters from fitting to the TRPL decay data.

Sample	A1	τ_1 [ns]	A2	τ_2 [ns]
Reference Spiro	0.41	1.24	0.29	18.26
TBU4-Cu	0.86	1.46	0.19	27.08
TBU4-Zn	0.24	1.68	0.23	30.11
TBU4-Co	0.43	2.11	0.18	69.37

The Spiro sample had the shortest PL decay time of 18.26 ns, indicating an effective charge transfer between it and the perovskite. The glass/perovskite/TBU4-Cu sample also had a faster decay time of 27.08 ns compared to TBU4-Zn (30.11 ns) and TBU4-Co (69.37 ns). This suggests a more efficient charge transfer at the interface between the perovskite film and Spiro. The passivation effect of the Spiro on the perovskite defects may be responsible for this, as it can prevent charge carriers from being trapped and impede charge transfer.

In order to determine the density of the defect states at the interface between the HTM and perovskite layer, hole-only devices (ITO/Meo/Perovskite/HTM/Au) were fabricated, and their electronic properties were analyzed, as reported in a previous study [56]. The dark J-V curves of the devices are shown in Figure 5, and the trap-state density (N_{trap}) was calculated using the equation proposed by Jacobsson et al.:

$$N_{\text{trap}} = 2V_{\text{TFL}} \epsilon_0 \epsilon / eL^2 \quad (1)$$

where N_{trap} , V_{TFL} , ϵ_0 , ϵ , e , L , are the trap-state density, the trap-filled limit voltage, vacuum permittivity ($\epsilon_0 = 8.8 \times 10^{-12} \text{ F m}^{-1}$), the relative dielectric constant of perovskite (62.23) [57], electron charge ($e = 1.6 \times 10^{-19} \text{ C}$), and the film thickness of perovskite (350 nm), respectively. Since the perovskite with different HTMs in the devices possesses the same ϵ_0 , ϵ , e , L , the magnitude of N_{trap} is only determined by the V_{TFL} . As shown in Figure 5, the V_{TFL} of the perovskites based on the reference Meo/Spiro, Meo/TBU4-Cu, Meo/TBU4-Zn, and Meo/TBU4-Co are 0.14 V, 0.17 V, 0.22 V, and 0.30 V respectively.

The perovskite film, with the phthalocyanine layers, shows a bit of a higher V_{TFL} than that of the Spiro sample, implying increased trap states. According to the result of V_{TFL} , the N_{trap} of the perovskites, based on the Spiro, Meo/TBU4-Cu, Meo/TBU4-Zn, and Meo/TBU4-Co are $2.74 \times 10^{15} \text{ cm}^{-3}$, $3.33 \times 10^{15} \text{ cm}^{-3}$, $4.31 \times 10^{15} \text{ cm}^{-3}$, and $5.88 \times 10^{15} \text{ cm}^{-3}$. This result further proves that the TBU4-Cu-based HTM devices can effectively reduce the defect density of perovskite.

Further, we have calculated the mobility of HTMs. The hole mobilities for all the HTMs are extracted from the space-charge limited current (SCLC) measurement using hole-only devices, respectively. For hole-only devices, the device architecture was ITO/Meo/Perovskite/HTMs/Ag. The SCLC mobilities were calculated using the Mott-Gurney equation [58]:

$$J = 9\epsilon_0\epsilon_r\mu_h V^2 / 8L^3$$

where $J = J$ is the current density, ϵ_r is the relative dielectric constant of the active layer material (usually 2–4 for organic semiconductor), herein we used a relative dielectric constant of 3.5, ϵ_0 is the permittivity of empty space ($8.8 \times 10^{-12} \text{ F m}^{-1}$), μ_h is the mobility of hole or electron, L is the thickness of the active layer 350 nm, and V is the applied voltage in the device.

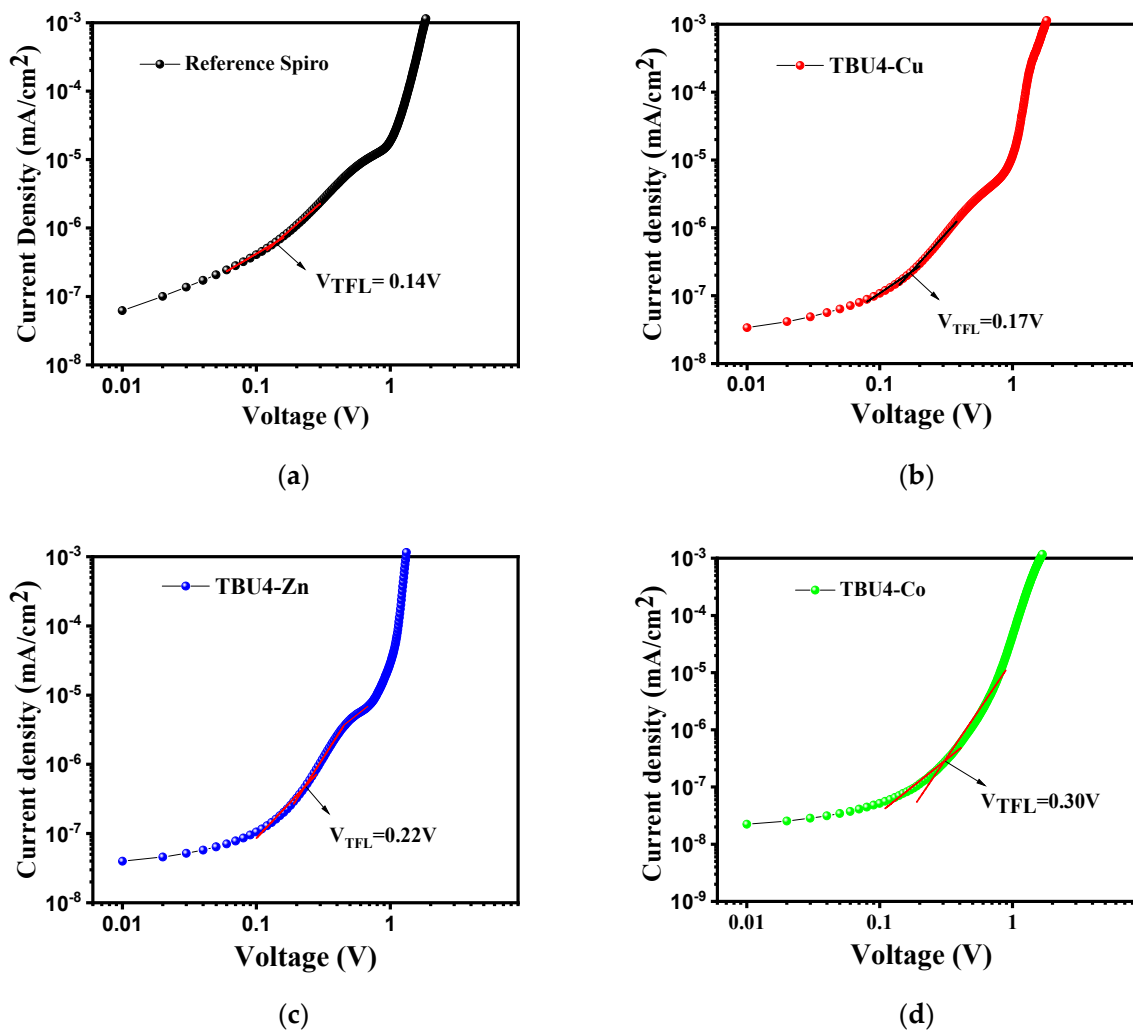


Figure 5. Space charge-limited current (SCLC) measurements of the hole-only devices. (ITO/Meo/Perovskite/HTM/Au device structure): (a) Reference-Spiro, (b) TBU4-Cu, (c) TBU4-Zn and (d) TBU4-Co.

The mobilities of TBU4-Cu, TBU4-Zn, and TBU4-Co were $3.39 \times 10^{-2} \text{ cm}^2 \text{ V}^{-1} \text{ S}^{-1}$, $2.36 \times 10^{-2} \text{ cm}^2 \text{ V}^{-1} \text{ S}^{-1}$, $1.24 \times 10^{-2} \text{ cm}^2 \text{ V}^{-1} \text{ S}^{-1}$ respectively, whereas the hole mobility of LiTFSI-doped Spiro is $2.45 \times 10^{-3} \text{ cm}^2 \text{ V}^{-1} \text{ s}^{-1}$ [59].

The SEM morphological images of the anisole-processed HTMs are reported in Figure 6. While TBU4-Cu and TBU4-Zn nicely cover the perovskite layer, the TBU4-Co films are not uniform due to the presence of pinholes. This evidence may be due to an incompatibility between cobalt and anisole during the spin-coating process, given the relevant impact that the central metal can have on the interactions between a phthalocyanine and the solvent. This might cause recombination or decrease the short circuit current of the device and explain the poorer performances of TBU4-Co as an HTM.

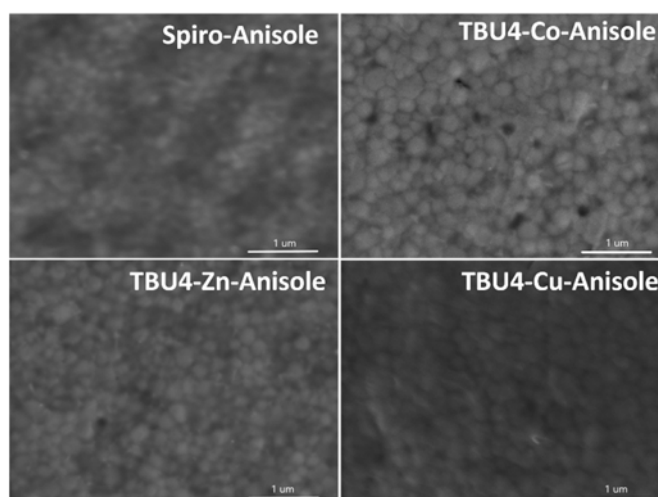


Figure 6. SEM morphological images of Spiro, TBU4-Co, TBU4-Zn, and TBU4-Cu deposited on perovskite film.

3.3. Cost Analysis

To evaluate the fabrication costs of our hole transport materials, we have performed a cost-per-gram analysis of our phthalocyanines, comparing the results with the current price of Spiro-MeOTAD and the commercially available counterparts of our molecules when present. It must be pointed out that, being an estimation, our analysis does not include parameters such as energy, facility maintenance and personnel costs, taxes, and other charges which are supposed to impact the final cost. The total material cost for our phthalocyanines has been calculated according to a paper published in 2013 by Osedach et al. [60], all the details are described in the Supplementary Materials. The resulting costs for the reagents, solvents, and purification materials are reported in Table 4 as Euro per gram of the synthesized product.

Table 4. Cost estimation of TBU4-Co, TBU4-Cu, TBU4-Zn. Commercial Spiro-MeOTAD (unsublimed, 99.0% purity) is included for comparison. Prices are given as EUR/g.

HTM	Reagents	Solvents	Workup/Purification	Total	Cheapest Price on Market
TBU4-Co	43.85	0.41	37.44	81.70	n/a
TBU4-Cu	24.66	0.22	1.70	26.58	124.00 ¹
TBU4-Zn	26.63	0.22	23.28	50.13	101.00 ¹
Spiro-MeOTAD	/	/	/	/	264.50 ²

¹ Sold by PorphyChem; ² Sold by Ossila.

As expected, the cobalt derivative is the most expensive, while TBU4-Cu is the cheapest. By dividing the total costs by reagents, solvents, and workup, it is easier to understand which part of the synthesis impacts the final price the most. The purification of cobalt and zinc phthalocyanines requires a filtration on silica gel which also implies the use of solvents and makes the cost of purification approximately equal to that of the reagents. Instead, the copper derivative is purified without the need for chromatography, with a positive impact on the final price. Noteworthy, these HTMs are not only much cheaper than Spiro-MeOTAD, which ranges approximately between 260–500 EUR/g depending on its purity and supplier, but also the commercial tetra-*tert*-butylphthalocyanines available on the market. Furthermore, it is worth pointing out the cost associated with the deposition solvent of our HTMs. Anisole is 2.5–3 times more expensive than chlorobenzene, so when preparing the solutions with a concentration of 10 mg/mL, the expense for the solvent is around 0.03 EUR for anisole and 0.01 EUR for chlorobenzene. Although apparently not significant enough for laboratory-scale applications, this data can have a relevant impact on the total cost of larger production runs.

4. Conclusions

We have successfully developed an alternative synthesis of tetra-*tert*-butylphthalocyanines using a mixture of low-impacting solvents. These phthalocyanines are processable in anisole, are cheaper than the benchmark Spiro-MeOTAD, and do not strictly require chemical doping to work as HTMs in perovskite solar cells. The achieved J-V parameters for the anisole-processed TBU4-Cu-based devices are comparable to those of the Spiro-based devices, even in the absence of chemical doping, and the results are highly reproducible. TBU4-Co performed poorly, probably because of the misalignment of energy the level with the gold counter electrode and a poor morphology of the resulting layer presumably due to unfavorable interactions with the anisole during the spin-coating process. The anisole-processed HTMs provided PCEs up to 12.27% for TBU4-Cu and 11.73% for TBU4-Zn. In both cases, the photovoltaic parameters are higher than those of the corresponding cells made with chlorobenzene, for which the best results obtained were, respectively, 12.22% and 10.81%. Remarkably, our combined approach to reduce the environmental and health impact of both the synthesis and deposition of the performing HTMs allowed us to identify TBU4-Cu as a promising molecular material for more environmentally sustainable perovskite solar cells.

Supplementary Materials: The following supporting information can be downloaded at: <https://www.mdpi.com/article/10.3390/en16093643/s1>, Figure S1: ¹H NMR of TBU4-Zn; Figure S2a: IR spectrum of TBU4-Co; Figure S2b: IR spectrum of TBU4-Cu; Figure S2c: IR spectrum of TBU4-Zn; Figure S3a: ESI-MS spectrum of TBU4-Co; Figure S3b: ESI-MS spectrum of TBU4-Cu; Figure S3c: ESI-MS spectrum of TBU4-Zn; Figure S4a: Cyclic voltammogram (anodic scan) of TBU4-Co; Figure S4b: Cyclic voltammogram (anodic scan) of TBU4-Cu; Figure S4c: Cyclic voltammogram (anodic scan) of TBU4-Zn; Table S1: Prices of quoted materials; Figure S5: Flowcharts for the syntheses of 1.000 g of target phthalocyanines; Figure S6: Solutions of various HTMs in chlorobenzene and anisole; Figure S7: UV-vis absorption spectra of TBU4-Co, TBU4-Zn, TBU4-Cu thin films on perovskite; Figure S8: Current density vs. voltage curves of anisole- and chlorobenzene-based HTM devices; Figure S9: Statistical evaluation box charts of anisole- and chlorobenzene-based devices; Figure S10: Surface morphologies with roughness values of target phthalocyanines.

Author Contributions: Conceptualization, S.K.P., L.M., G.Z. and T.M.B.; methodology, S.K.P. and L.M.; validation, S.K.P. and L.M.; formal analysis, S.K.P. and L.M.; investigation, S.K.P., L.M., J.X. and S.H.R.; resources, G.Z., A.D.C. and T.M.B.; data curation, S.K.P. and L.M.; writing—original draft preparation, S.K.P. and L.M.; writing—review and editing, S.K.P., L.M., J.X., S.H.R., A.D.C., G.Z. and T.M.B.; visualization, S.K.P., L.M., G.Z., J.X. and S.H.R.; supervision, G.Z., A.D.C. and T.M.B.; project administration, G.Z. and T.M.B.; funding acquisition, G.Z., A.D.C. and T.M.B. All authors have read and agreed to the published version of the manuscript.

Funding: This research was funded by MIUR through grant PRIN2017 BOOSTER (protocol number 2017YXX8AZ) and Lazio Region through ISIS@MACH (IR approved by Giunta Regionale n. G10795, 7 August 2019) published by BURL n. 69 27 August 2019.

Data Availability Statement: The data presented in this study are available in this article and in the Supplementary Materials file.

Acknowledgments: G.Z. and L.M. thank Anna Maria Paoletti, Giovanna Pennesi and Venanzio Raglione for fruitful scientific discussions.

Conflicts of Interest: The authors declare no conflict of interest.

References

1. Kojima, A.; Teshima, K.; Shirai, Y.; Miyasaka, T. Organometal Halide Perovskites as Visible-Light Sensitizers for Photovoltaic Cells. *J. Am. Chem. Soc.* **2009**, *131*, 6050–6051. [[CrossRef](#)] [[PubMed](#)]
2. Green, M.A.; Dunlop, E.D.; Hohl-Ebinger, J.; Yoshita, M.; Kopidakis, N.; Hao, X. Solar Cell Efficiency Tables (Version 59). *Prog. Photovolt. Res. Appl.* **2022**, *30*, 3–12. [[CrossRef](#)]
3. Rong, Y.; Hu, Y.; Mei, A.; Tan, H.; Saidaminov, M.I.; Seok, S.I.; McGehee, M.D.; Sargent, E.H.; Han, H. Challenges for Commercializing Perovskite Solar Cells. *Science* **2018**, *361*, eaat8235. [[CrossRef](#)] [[PubMed](#)]

4. Abate, A.; Correa-Baena, J.P.; Saliba, M.; Su'ait, M.S.; Bella, F. Perovskite Solar Cells: From the Laboratory to the Assembly Line. *Chem. Eur. J.* **2018**, *24*, 3083–3100. [[CrossRef](#)] [[PubMed](#)]
5. Abate, A.; Hollman, D.J.; Teuscher, J.; Pathak, S.; Avolio, R.; D'Errico, G.; Vitiello, G.; Fantacci, S.; Snaith, H.J. Protic Ionic Liquids as P-Dopant for Organic Hole Transporting Materials and Their Application in High Efficiency Hybrid Solar Cells. *J. Am. Chem. Soc.* **2013**, *135*, 13538–13548. [[CrossRef](#)]
6. Snaith, H.J.; Grätzel, M. Enhanced Charge Mobility in a Molecular Hole Transporter via Addition of Redox Inactive Ionic Dopant: Implication to Dye-Sensitized Solar Cells. *Appl. Phys. Lett.* **2006**, *89*, 262114. [[CrossRef](#)]
7. Abate, A.; Leijtens, T.; Pathak, S.; Teuscher, J.; Avolio, R.; Errico, M.E.; Kirkpatrick, J.; Ball, J.M.; Docampo, P.; McPherson, I.; et al. Lithium Salts as “Redox Active” p-Type Dopants for Organic Semiconductors and Their Impact in Solid-State Dye-Sensitized Solar Cells. *Phys. Chem. Chem. Phys.* **2013**, *15*, 2572–2579. [[CrossRef](#)]
8. Nguyen, W.H.; Bailie, C.D.; Unger, E.L.; McGehee, M.D. Enhancing the Hole-Conductivity of Spiro-OMeTAD without Oxygen or Lithium Salts by Using Spiro(TFSI)₂ in Perovskite and Dye-Sensitized Solar Cells. *J. Am. Chem. Soc.* **2014**, *136*, 10996–11001. [[CrossRef](#)]
9. Liu, J.; Pathak, S.; Stergiopoulos, T.; Leijtens, T.; Wojciechowski, K.; Schumann, S.; Kausch-Busies, N.; Snaith, H.J. Employing PEDOT as the P-Type Charge Collection Layer in Regular Organic-Inorganic Perovskite Solar Cells. *J. Phys. Chem. Lett.* **2015**, *6*, 1666–1673. [[CrossRef](#)]
10. Kumar, C.V.; Sfyri, G.; Raptis, D.; Stathatos, E.; Lianos, P. Perovskite Solar Cell with Low Cost Cu-Phthalocyanine as Hole Transporting Material. *RSC Adv.* **2015**, *5*, 3786–3791. [[CrossRef](#)]
11. Urbani, M.; de La Torre, G.; Nazeeruddin, M.K.; Torres, T. Phthalocyanines and Porphyrinoid Analogues as Hole-and Electron-Transporting Materials for Perovskite Solar Cells. *Chem. Soc. Rev.* **2019**, *48*, 2738–2766. [[CrossRef](#)] [[PubMed](#)]
12. Duong, T.; Peng, J.; Walter, D.; Xiang, J.; Shen, H.; Chugh, D.; Lockrey, M.; Zhong, D.; Li, J.; Weber, K.; et al. Perovskite Solar Cells Employing Copper Phthalocyanine Hole-Transport Material with an Efficiency over 20% and Excellent Thermal Stability. *ACS Energy Lett.* **2018**, *3*, 2441–2448. [[CrossRef](#)]
13. Cho, K.T.; Rakstys, K.; Cavazzini, M.; Orlandi, S.; Pozzi, G.; Nazeeruddin, M.K. Perovskite Solar Cells Employing Molecularly Engineered Zn(II) Phthalocyanines as Hole-Transporting Materials. *Nano Energy* **2016**, *30*, 853–857. [[CrossRef](#)]
14. Feng, Y.; Hu, Q.; Rezaee, E.; Li, M.; Xu, Z.X.; Lorenzoni, A.; Mercuri, F.; Muccini, M. High-Performance and Stable Perovskite Solar Cells Based on Dopant-Free Arylamine-Substituted Copper(II) Phthalocyanine Hole-Transporting Materials. *Adv. Energy Mater.* **2019**, *9*, 1901019. [[CrossRef](#)]
15. Yu, Z.; Hagfeldt, A.; Sun, L. The Application of Transition Metal Complexes in Hole-Transporting Layers for Perovskite Solar Cells: Recent Progress and Future Perspectives. *Coord. Chem. Rev.* **2020**, *406*, 213143. [[CrossRef](#)]
16. Qu, G.; Dong, L.; Qiao, Y.; Khan, D.; Chen, Q.; Xie, P.; Yu, X.; Liu, X.; Wang, Y.; Chen, J.; et al. Dopant-Free Phthalocyanine Hole Conductor with Thermal-Induced Holistic Passivation for Stable Perovskite Solar Cells with 23% Efficiency. *Adv. Funct. Mater.* **2022**, *32*, 2206585. [[CrossRef](#)]
17. Li, D.; Ge, S.; Yuan, T.; Gong, J.; Huang, B.; Tie, W.; He, W. Green Synthesis and Characterization of Crystalline Zinc Phthalocyanine and Cobalt Phthalocyanine Prisms by a Simple Solvothermal Route. *CrystEngComm* **2018**, *20*, 2749–2758. [[CrossRef](#)]
18. Li, D.; Zhang, P.; Ge, S.; Sun, G.; He, Q.; Fa, W.; Li, Y.; Ma, J. A Green Route to Prepare Metal-Free Phthalocyanine Crystals with Controllable Structures by a Simple Solvothermal Method. *RSC Adv.* **2021**, *11*, 31226–31234. [[CrossRef](#)]
19. Langerreiter, D.; Kostianen, M.A.; Kaabel, S.; Anaya-Plaza, E. A Greener Route to Blue: Solid-State Synthesis of Phthalocyanines. *Angew. Chem. Int. Ed.* **2022**, *61*, e202209033. [[CrossRef](#)]
20. Koyun, Ö.; Gördük, S.; Keskin, B.I.; Çetinkaya, A.; Koca, A.I.; Avciata, U. Microwave-Assisted Synthesis, Electrochemistry and Spectroelectrochemistry of Phthalocyanines Bearing Tetra Terminal-Alkynyl Functionalities and Click Approach. *Polyhedron* **2016**, *113*, 35–49. [[CrossRef](#)]
21. Abe, K.; Katano, S.; Ohta, K. Microwave-Assisted Synthesis of Phthalocyanine Metal Complexes: Relationship between Yield and Maximum Temperature Reached by Microwave Irradiation. *J. Jpn. Pet. Inst.* **2018**, *61*, 140–149. [[CrossRef](#)]
22. Shaabani, A.; Maleki-Moghaddam, R.; Maleki, A.; Rezayan, A.H. Microwave Assisted Synthesis of Metal-Free Phthalocyanine and Metallophthalocyanines. *Dye. Pigment.* **2007**, *74*, 279–282. [[CrossRef](#)]
23. Burczyk, A.; Loupy, A.; Bogdal, D.; Petit, A. Improvement in the Synthesis of Metallophthalocyanines Using Microwave Irradiation. *Tetrahedron* **2005**, *61*, 179–188. [[CrossRef](#)]
24. Villemin, D.; Hammadi, M.; Hachemi, M.; Bar, N. Applications of Microwave in Organic Synthesis: An Improved One-Step Synthesis of Metallophthalocyanines and a New Modified Microwave Oven for Dry Reactions. *Molecules* **2001**, *6*, 831–844. [[CrossRef](#)]
25. Gonzalez, A.C.S.; Damas, L.; Aroso, R.T.; Tomé, V.A.; Dias, L.D.; Pina, J.; Carrilho, R.M.B.; Pereira, M.M. Monoterpene-Based Metallophthalocyanines: Sustainable Synthetic Approaches and Photophysical Studies. *J. Porphyr. Phthalocyanines* **2020**, *24*, 947–958. [[CrossRef](#)]
26. Saito, Y.; Higuchi, T.; Sugimori, H.; Yabu, H. One-Pot UV-Assisted Synthesis of Metal Phthalocyanine Nanocrystals. *ChemNanoMat* **2015**, *1*, 92–95. [[CrossRef](#)]
27. Youssef, T.E. Efficient Green Procedures for the Preparation of Novel Tetraalkynyl-Substituted Phthalocyanines. *Polyhedron* **2010**, *29*, 1776–1783. [[CrossRef](#)]

28. Lo, P.C.; Cheng, D.Y.Y.; Ng, D.K.P. Phthalocyanine Synthesis in Ionic Liquids: Preparation of Differently Substituted Phthalocyanines in Tetrabutylammonium Bromide. *Synthesis* **2005**, *2005*, 1141–1147. [[CrossRef](#)]
29. Yadav, K.K.; Poonam, P.; Chauhan, S.M.S. Convenient and Efficient Method for the Synthesis of Phthalocyanines and Metallophthalocyanines in Task-Specific 2-Hydroxyethyl Ionic Liquids. *Synth. Commun.* **2014**, *44*, 2797–2807. [[CrossRef](#)]
30. Shaabani, A.; Hooshmand, S.E.; Afshari, R.; Shaabani, S.; Ghasemi, V.; Atharnezhad, M.; Akbari, M. Direct Construction of Diverse Metallophthalocyanines by Manifold Substrates in a Deep Eutectic Solvent. *J. Solid. State Chem.* **2018**, *258*, 536–542. [[CrossRef](#)]
31. Zanotti, G.; Imperatori, P.; Paoletti, A.M.; Pennesi, G. Sustainable Approaches to the Synthesis of Metallophthalocyanines in Solution. *Molecules* **2021**, *26*, 1760. [[CrossRef](#)] [[PubMed](#)]
32. Zanotti, G.; Angelini, N.; Mattioli, G.; Paoletti, A.M.; Pennesi, G.; Caschera, D.; Sobolev, A.P.; Beverina, L.; Calascibetta, A.M.; Sanzone, A.; et al. [1]Benzothieno[3,2-b][1]Benzothiophene-Phthalocyanine Derivatives: A Subclass of Solution-Processable Electron-Rich Hole Transport Materials. *Chempluschem* **2020**, *85*, 2376–2386. [[CrossRef](#)]
33. Bernt, C.M.; Bottari, G.; Barrett, J.A.; Scott, S.L.; Barta, K.; Ford, P.C. Mapping Reactivities of Aromatic Models with a Lignin Disassembly Catalyst. Steps toward Controlling Product Selectivity. *Catal. Sci. Technol.* **2016**, *6*, 2984–2994. [[CrossRef](#)]
34. Gillet, S.; Aguedo, M.; Petitjean, L.; Morais, A.R.C.; da Costa Lopes, A.M.; Łukasik, R.M.; Anastas, P.T. Lignin Transformations for High Value Applications: Towards Targeted Modifications Using Green Chemistry. *Green Chem.* **2017**, *19*, 4200–4233. [[CrossRef](#)]
35. Leiva, K.; Garcia, R.; Sepulveda, C.; Laurenti, D.; Geantet, C.; Vrinat, M.; Garcia-Fierro, J.L.; Escalona, N. Conversion of Guaiacol over Supported ReOx Catalysts: Support and Metal Loading Effect. *Catal. Today* **2017**, *296*, 228–238. [[CrossRef](#)]
36. Byrne, F.P.; Jin, S.; Paggiola, G.; Petchey, T.H.M.; Clark, J.H.; Farmer, T.J.; Hunt, A.J.; Robert McElroy, C.; Sherwood, J. Tools and Techniques for Solvent Selection: Green Solvent Selection Guides. *Sustain. Chem. Process.* **2016**, *4*, 7. [[CrossRef](#)]
37. Restrepo, J.B.; Paternina-Arboleda, C.D.; Bula, A.J. 1,2-Propanediol Production from Glycerol Derived from Biodiesel's Production: Technical and Economic Study. *Energies* **2021**, *14*, 81. [[CrossRef](#)]
38. Mondal, S.; Arifa, A.A.; Biswas, P. Production of 1,2-Propanediol from Renewable Glycerol Over Highly Stable and Efficient Cu–Zn(4:1)/MgO Catalyst. *Catal. Letters* **2017**, *147*, 2783–2798. [[CrossRef](#)]
39. Tao, Y.m.; Bu, C.y.; Zou, L.h.; Hu, Y.l.; Zheng, Z.J.; Ouyang, J. A Comprehensive Review on Microbial Production of 1,2-Propanediol: Micro-Organisms, Metabolic Pathways, and Metabolic Engineering. *Biotechnol. Biofuels* **2021**, *14*, 216. [[CrossRef](#)]
40. Taylor, A.D.; Sun, Q.; Goetz, K.P.; An, Q.; Schramm, T.; Hofstetter, Y.; Litterst, M.; Paulus, F.; Vaynzof, Y. A General Approach to High-Efficiency Perovskite Solar Cells by Any Antisolvent. *Nat. Commun.* **2021**, *12*, 1878. [[CrossRef](#)]
41. Yavari, M.; Mazloum-Ardakani, M.; Gholipour, S.; Tavakoli, M.M.; Turren-Cruz, S.H.; Taghavinia, N.; Grätzel, M.; Hagfeldt, A.; Saliba, M. Greener, Nonhalogenated Solvent Systems for Highly Efficient Perovskite Solar Cells. *Adv. Energy Mater.* **2018**, *8*, 1800177. [[CrossRef](#)]
42. Zhao, P.; Kim, B.J.; Ren, X.; Lee, D.G.; Bang, G.J.; Jeon, J.B.; Kim, W.b.; Jung, H.S. Antisolvent with an Ultrawide Processing Window for the One-Step Fabrication of Efficient and Large-Area Perovskite Solar Cells. *Adv. Mater.* **2018**, *30*, 1802763. [[CrossRef](#)] [[PubMed](#)]
43. Wang, L.; Wang, X.; Deng, L.L.; Leng, S.; Guo, X.; Tan, C.H.; Choy, W.C.H.; Chen, C.C. The Mechanism of Universal Green Antisolvents for Intermediate Phase Controlled High-Efficiency Formamidinium-Based Perovskite Solar Cells. *Mater. Horiz.* **2020**, *7*, 934–942. [[CrossRef](#)]
44. de Rossi, F.; Pontecorvo, T.; Brown, T.M. Characterization of Photovoltaic Devices for Indoor Light Harvesting and Customization of Flexible Dye Solar Cells to Deliver Superior Efficiency under Artificial Lighting. *Appl. Energy* **2015**, *156*, 413–422. [[CrossRef](#)]
45. Henriques, C.A.; Pinto, S.M.A.; Aquino, G.L.B.; Pineiro, M.; Calvete, M.J.F.; Pereira, M.M. Ecofriendly Porphyrin Synthesis by Using Water under Microwave Irradiation. *ChemSusChem* **2014**, *7*, 2821–2824. [[CrossRef](#)]
46. Gomes, C.; Peixoto, M.; Pineiro, M. Porphyrin Synthesis Using Mechanochemistry: Sustainability Assessment. *J. Porphyr. Phthalocyanines* **2019**, *23*, 889–897. [[CrossRef](#)]
47. Calvete, M.J.F.; Dias, L.D.; Henriques, C.A.; Pinto, S.M.A.; Carrilho, R.M.B.; Pereira, M.M. A Cost-Efficient Method for Unsymmetrical Meso-Aryl Porphyrin Synthesis Using NaY Zeolite as an Inorganic Acid Catalyst. *Molecules* **2017**, *22*, 741. [[CrossRef](#)]
48. Zanotti, G.; Mancini, L.; Paoletti, A.M.; Pennesi, G.; Raglione, V. Greener Shades of Blue: Green Chemistry as an Opportunity to Improve the Approach to the Synthesis of Phthalocyanines. *J. Porphyr. Phthalocyanines* **2023**. [[CrossRef](#)]
49. Lin, Z.; Chang, J.; Xiao, J.; Zhu, H.; Xu, Q.H.; Zhang, C.; Ouyang, J.; Hao, Y. Interface Studies of the Planar Heterojunction Perovskite Solar Cells. *Sol. Energy Mater. Sol. Cells* **2016**, *157*, 783–790. [[CrossRef](#)]
50. Jacobsson, T.J.; Hultqvist, A.; García-Fernández, A.; Anand, A.; Al-Ashouri, A.; Hagfeldt, A.; Crovetto, A.; Abate, A.; Ricciardulli, A.G.; Vijayan, A.; et al. An Open-Access Database and Analysis Tool for Perovskite Solar Cells Based on the FAIR Data Principles. *Nat. Energy* **2022**, *7*, 107–115. [[CrossRef](#)]
51. Javier Ramos, F.; Ince, M.; Urbani, M.; Abate, A.; Grätzel, M.; Ahmad, S.; Torres, T.; Nazeeruddin, M.K. Non-Aggregated Zn(II)Octa(2,6-Diphenylphenoxy) Phthalocyanine as a Hole Transporting Material for Efficient Perovskite Solar Cells. *Dalton Trans.* **2015**, *44*, 10847–10851. [[CrossRef](#)] [[PubMed](#)]
52. Liao, P.; Zhao, X.; Li, G.; Shen, Y.; Wang, M. A New Method for Fitting Current–Voltage Curves of Planar Heterojunction Perovskite Solar Cells. *Nanomicro Lett.* **2018**, *10*, 5. [[CrossRef](#)] [[PubMed](#)]

53. Babu, V.; Fuentes Pineda, R.; Ahmad, T.; Alvarez, A.O.; Castriotta, L.A.; di Carlo, A.; Fabregat-Santiago, F.; Wojciechowski, K. Improved Stability of Inverted and Flexible Perovskite Solar Cells with Carbon Electrode. *ACS Appl. Energy Mater.* **2020**, *3*, 5126–5134. [[CrossRef](#)]
54. Saranin, D.; Komaricheva, T.; Luchnikov, L.; Muratov, D.S.; Le, T.S.; Karpov, Y.; Gostishchev, P.; Yurchuk, S.; Kuznetsov, D.; Didenko, S.; et al. Hysteresis-Free Perovskite Solar Cells with Compact and Nanoparticle NiO for Indoor Application. *Sol. Energy Mater. Sol. Cells* **2021**, *227*, 111095. [[CrossRef](#)]
55. Zhu, Z.; Bai, Y.; Lee, H.K.H.; Mu, C.; Zhang, T.; Zhang, L.; Wang, J.; Yan, H.; So, S.K.; Yang, S. Polyfluorene Derivatives Are High-Performance Organic Hole-Transporting Materials for Inorganic–Organic Hybrid Perovskite Solar Cells. *Adv. Funct. Mater.* **2014**, *24*, 7357–7365. [[CrossRef](#)]
56. Li, X.; Li, W.; Yang, Y.; Lai, X.; Su, Q.; Wu, D.; Li, G.; Wang, K.; Chen, S.; Sun, X.W.; et al. Defects Passivation with Dithienobenzodithiophene-Based π -Conjugated Polymer for Enhanced Performance of Perovskite Solar Cells. *Solar RRL* **2019**, *3*, 1900029. [[CrossRef](#)]
57. Hu, X.; Wang, H.; Wang, M.; Zang, Z. Interfacial Defects Passivation Using Fullerene-Polymer Mixing Layer for Planar-Structure Perovskite Solar Cells with Negligible Hysteresis. *Solar Energy* **2020**, *206*, 816–825. [[CrossRef](#)]
58. Abbaszadeh, D.; Kunz, A.; Wetzelaer, G.A.H.; Michels, J.J.; Craciun, N.I.; Koynov, K.; Lieberwirth, I.; Blom, P.W.M. Elimination of Charge Carrier Trapping in Diluted Semiconductors. *Nat. Mater.* **2016**, *15*, 628–633. [[CrossRef](#)]
59. Ren, G.; Han, W.; Deng, Y.; Wu, W.; Li, Z.; Guo, J.; Bao, H.; Liu, C.; Guo, W. Strategies of Modifying Spiro-OMeTAD Materials for Perovskite Solar Cells: A Review. *J. Mater. Chem. A Mater.* **2021**, *9*, 4589–4625. [[CrossRef](#)]
60. Osedach, T.P.; Andrew, T.L.; Bulović, V. Effect of Synthetic Accessibility on the Commercial Viability of Organic Photovoltaics. *Energy Environ. Sci.* **2013**, *6*, 711–718. [[CrossRef](#)]

Disclaimer/Publisher’s Note: The statements, opinions and data contained in all publications are solely those of the individual author(s) and contributor(s) and not of MDPI and/or the editor(s). MDPI and/or the editor(s) disclaim responsibility for any injury to people or property resulting from any ideas, methods, instructions or products referred to in the content.